Elastic-invisibility-enabled metastructure with mechanically programmed nonlinear resonators for vibration attenuation and energy harvesting

João Pedro Norenberg[1,2,3], Americo Cunha Jr.[4,5], Diego Misseroni[2]

[1]Department of Mechanical Engineering, São Paulo State University, Ilha Solteira-SP, 15385-007, Brazil.

[2]Department of Civil, Environmental and Mechanical Engineering, University of Trento, Trento, 38123, Italy.

[3]Department of Mechanical Engineering, University of São Paulo, São Carlos-SP, 13566-590, Brazil.

[4]Institute of Mathematics and Statistics, Rio de Janeiro State University, Rio de Janeiro - RJ, 20950-000, Brazil.

[5]National Laboratory of Scientific Computing, Petrópolis - RJ, 25651-075, Brazil.

*E-mails: jp.norenberg@usp.br (J.P.N.), americo@lncc.br (A.C.)
and diego.misseroni@unitn.it (D.M.)

Mechanical programming provides a simple way to tune embedded nonlinear resonators without redesigning the host structure. Here, seven magneto-piezoelectric resonators are integrated into elastically reconstructed openings of a host beam. The removed stiffness, mass, and inertia are restored. The dynamics of the intact beam are therefore recovered over the investigated frequency range. Programming is performed by changing only the spacing between repulsive magnets. Each resonator can be set independently. This creates uniform, nonuniform, and graded combinations of monostable and bistable states. Experiments and simulations show marked changes in both vibration attenuation and harvested power. Different programs favor different functions. One configuration reaches 1.82 times the reference attenuation bandwidth. Another reaches 1.57 times the reference harvesting performance. Assuming nine admissible states per resonator, the seven-resonator system spans 9^7 possible configurations. Model-selected candidates improve both numerical references simultaneously, reaching 1.16 times the attenuation bandwidth and 1.11 times the harvesting metric. The prototype also delivers up to 10.67 μW of total AC load power near resonance. The result is a structurally integrated platform with programmable nonlinear functionality and largely preserved host dynamics.

Keywords: metamaterial | elastic wave manipulation | nonlinear dynamics | power generation

1 Introduction

Unwanted structural vibrations degrade performance, accelerate fatigue, generate noise, and compromise the reliability of engineering systems. At the same time, these vibrations represent an abundant source of ambient mechanical energy that can be converted into electricity through piezoelectric, triboelectric, electromagnetic, or hybrid transduction mechanisms (*1–4*). This has motivated the development of multifunctional systems that use the same vibration field for attenuation and energy harvesting. Such systems are attractive in aerospace, transportation, civil infrastructure, and industrial applications. Vibration suppression can improve structural reliability, while harvested energy can support autonomous sensors in locations where wiring or battery replacement is difficult (*5, 6*).

Mechanical metamaterials and metastructures provide a powerful framework for achieving this multifunctionality through the deliberate manipulation of elastic-wave propagation (*7–16*). In particular, locally resonant metamaterials generate frequency bandgaps that inhibit wave propagation while concentrating mechanical energy within resonant substructures (*17–19*). This localized energy can facilitate electromechanical conversion and has motivated numerous dual-functional metastructures based on defect-mode engineering (*20, 21*), triboelectric nanogenerators (*22*), nonlinear piezoelectric resonator arrays (*23–25*), electromagnetic resonators (*26*), and architected or additive-manufactured structures (*27*). Existing approaches, however, still face several practical limitations. Many operate over narrow frequency ranges or offer limited tunability, while others rely on externally attached resonators or comparatively complex architectures. Attenuation and harvesting may also compete with one another (see Supplementary Table S1).

A fundamental challenge underlying these limitations is the integration of resonant functionalities into a structural host beam without perturbing the host dynamics. Externally mounted resonators provide an effective route to locally resonant bandgaps (*24, 28, 29*). However, their placement outside the structural core adds external bulk and eccentric inertial loading, which can break geometric symmetry, induce parasitic modal coupling, and distort the targeted dynamic response. Embedding resonators inside the structural core offers a more compact and mechanically integrated alternative (*30–33*). However, this internal integration requires voids that locally modify the stiffness, mass, and mass moment of inertia of the host structure. These geometric discontinuities can introduce additional scattering and alter the background dynamics, making it difficult to separate the desired resonator-driven response from parasitic effects caused by the structural modification itself.

Elastic invisibility offers a mechanics-based route for embedding resonators while preserving the effective dynamics of the host. Originally developed to suppress wave scattering from defects or inclusions (*34–37*), invisibility concepts are reinterpreted here as a strategy for functional integration rather than concealment. Here, the voids are mechanically reconstructed and used as internal regions for resonator integration. By restoring the bending and torsional stiffnesses, mass,

and mass moment of inertia removed from the original structure, elastic reconstruction produces a host that is geometrically modified yet dynamically preserved. The reconstructed regions can then accommodate the resonators while reducing the dynamic perturbation caused by the voids themselves. Reduced scattering also leaves more of the propagating mechanical energy available to excite the resonators and their piezoelectric transducers.

The second element of the design is the nonlinear magneto-elastic resonator. Nonlinear resonators can broaden effective operational bandwidths for vibration attenuation and energy harvesting, enhance energy localization, and produce amplitude-dependent dynamic regimes that are inaccessible to linear resonators (*27, 30, 38–45*). In the present metastructure, the restoring force of each resonator is governed by the spacing between repulsive permanent magnets. Adjusting this spacing reshapes the local potential energy landscape, enabling transitions between monostable and bistable configurations without modifying the resonator architecture. The resulting nonlinear states shift the attenuation bands and modify the harvested-power spectrum.

This work establishes some conceptual advances. Elastic invisibility is introduced as a functional-integration principle for embedding resonators into structural hosts while preserving their effective dynamics. The nonlinear state of the resonator array is then independently prescribed by the magnet spacing vector $\mathbf{d}_i = [d_1, \ldots, d_j, \ldots, d_S]$, where i labels a programmed metastructure configuration, S is the number of embedded resonators, and d_j defines the magnet spacing assigned to the j-th resonator in that configuration. Each vector $\mathbf{d}_i$ therefore acts as a mechanical program for the resonator array. Independent control of d_j allows identical, nonidentical, and graded configurations within the same metastructure. Related spatial grading strategies have been explored in rainbow trapping and topological energy localization (*46–52*). Elastic reconstruction and independent resonator tuning therefore address different parts of the problem. The reconstruction limits the disturbance introduced by the internal openings, while the magnet spacing controls whether the resulting response favors attenuation, harvesting, or a compromise between the two.

The experimental metastructure consists of a host beam containing seven uniformly distributed internal voids (Fig. 1A). Each void houses a nonlinear magneto-elastic piezoelectric resonator (Fig. 1B), and bimorph piezoelectric patches convert local resonator strain into electrical output (Fig. 1C). The voids are elastically reconstructed to restore the effective dynamic response of the intact host, in contrast to uncloaked voids that perturb wave propagation (Fig. 1D). In the identical monostable state with a magnet spacing of 7 mm, the prototype powers multiple LEDs near the first host-beam resonance and within the bandgap, demonstrating simultaneous energy harvesting and vibration attenuation (Fig. 1E and Movie S1). In this state, under fixed-frequency excitation at 6 g, it delivers 10.67 μW of total AC harvested power near resonance at 29 Hz and 2.05 μW inside the bandgap at 41 Hz. Although the harvested power is lower inside the bandgap, multiple LEDs remain powered while vibration transmission through the host is suppressed. After rectification and storage, power at this level could support duty-cycled measurements using ultra-low-power sensing

electronics, as discussed in the Supplementary Text. Experiments supported by validated numerical simulations further show that magnet spacing control reconfigures the attenuation and harvesting spectra, allowing nonidentical configurations to produce distinct multifunctional response profiles.

2 Results

2.1 Elastic invisibility of the two-opening regions

The elastic reconstruction is designed around the geometry required to integrate each piezoelectric resonator into the host beam. The beam contains seven rectangular regions of 118×30 mm^2. A transverse crossbar of width $b_c = 7$ mm is retained inside each region to clamp the resonator, as shown in Fig. 1D. This crossbar divides the original opening into a small 8×30 mm^2 opening and a larger 103×30 mm^2 opening. The small opening provides access to the piezoelectric connections, whereas the large one contains the resonator. The reconstruction is therefore developed for this two-opening geometry rather than for a single rectangular void. Removing material from the beam changes the local bending and torsional stiffnesses, mass, and mass moments of inertia. The aim of the reconstruction is to recover these quantities while keeping the two openings and the crossbar needed for the resonator. Reinforcement layers are bonded symmetrically to both faces of the beam. The two openings share the longitudinal reinforcement width b_y and thickness h_t, while separate transverse widths $b_{x,1}$ and $b_{x,2}$ are used because the openings have different lengths. For the stiffness calculation, the two openings are represented by adjacent orthogonal grids. The crossbar is included in this representation and contributes directly to the stiffness of the reconstructed region. For each opening $k = 1, 2$, the equivalent flexural and torsional rigidities are required to match those of the corresponding intact part of the beam. The reconstruction conditions can be written as

$$D_{x,k} = D_{y,k} = H_k = D_p, \qquad k = 1, 2, \tag{1}$$

where

$$D_p = \frac{E_p h^3}{12\left(1 - \nu_p^2\right)} \tag{2}$$

is the flexural rigidity of the intact reference region. Here, $D_{x,k}$ and $D_{y,k}$ are the equivalent flexural rigidities of the k-th grid, while H_k represents its torsional contribution. These quantities depend on the dimensions of the reinforcement members and on the geometry of the corresponding opening. The prescribed dimensions of the openings and the crossbar are kept fixed, while $b_{x,1}$, $b_{x,2}$, b_y, and h_t are obtained numerically from the stiffness-equivalence conditions. The full grid formulation and the resulting reinforcement dimensions are given in the Supplementary Text (*53, 54*).

Matching the stiffnesses alone is not sufficient because the reinforcement also changes the local mass distribution. The inertial properties are therefore recovered separately. The inertial properties

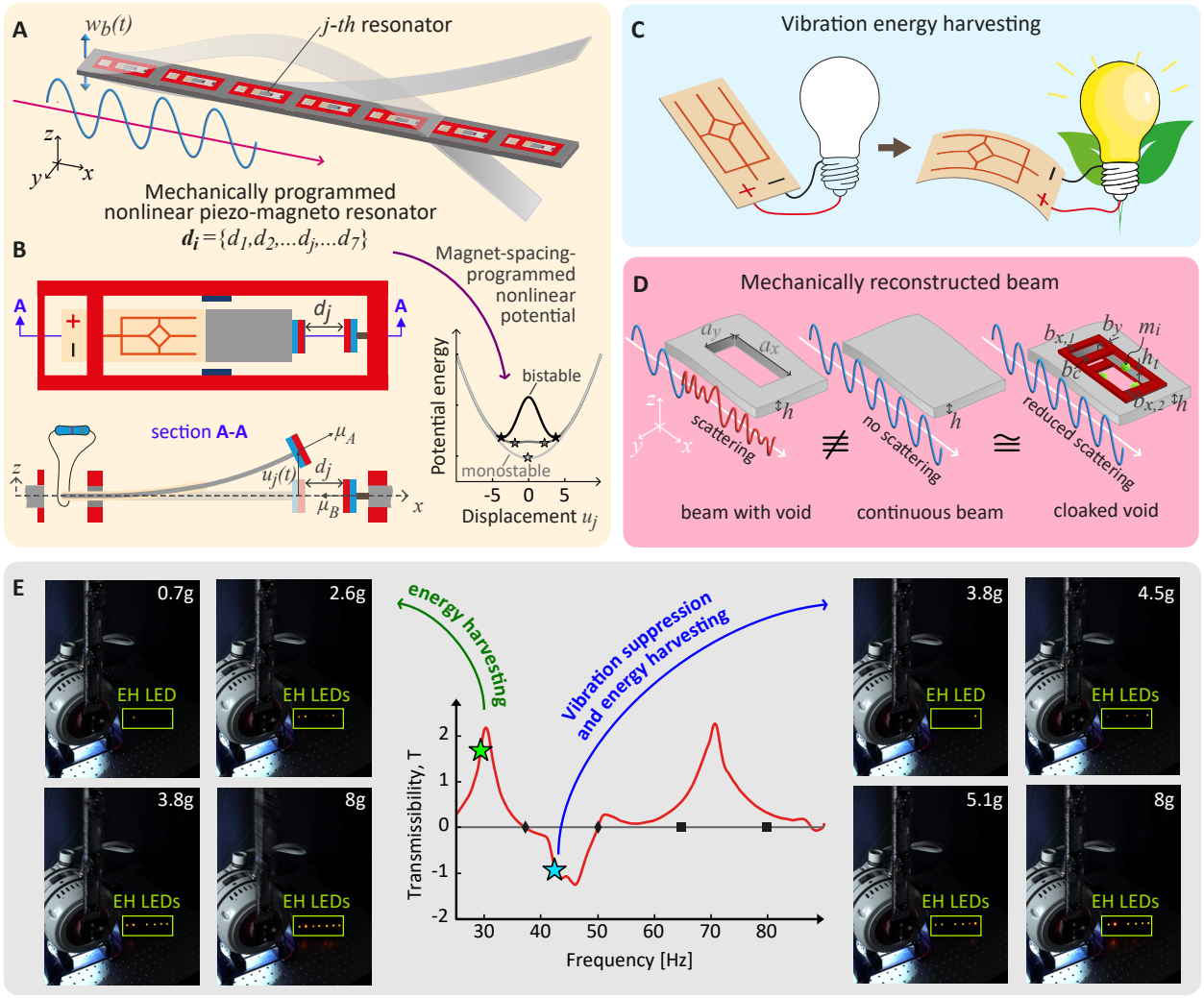


Figure 1: **Elastic-invisibility-enabled metastructure for energy harvesting and vibration attenuation**. (**A**) Cantilever beam with seven uniformly distributed internal voids hosting mechanically programmed nonlinear magneto-elastic piezoelectric resonators. The superimposed gray shapes indicate the first two bending modes of the host beam. (**B**) Embedded magneto-elastic piezoelectric resonator. The magnet spacing d_j controls the local nonlinear potential energy landscape, enabling monostable or bistable configurations. Section A–A shows the lateral view of the resonator and the repulsive magnetic interaction. (**C**) Piezoelectric energy harvesting mechanism for converting resonator strain into electrical output. (**D**) Elastic-invisibility strategy, where the uncloaked void scatters elastic waves while the cloaked void is mechanically reconstructed to recover the effective dynamic response of the intact host beam. (**E**) Energy harvesting (EH) LED demonstration for the identical monostable configuration at 7 mm, showing LED operation under different input accelerations both near resonance and within the vibration bandgap, where host vibration is suppressed.

of the small and large openings are evaluated about their respective local centroidal axes y_1 and y_2. For each reconstructed region, discrete masses are added to compensate the remaining differences in mass and principal mass moments of inertia. The corresponding conditions are

$$M_{p,k} = M_k + \sum_{i \in \mathcal{I}_k} m_i, \tag{3}$$

and

$$\begin{aligned} I_{p,k,x} &= I_{k,x} + \sum_{i \in \mathcal{I}_k} m_i \tilde{d}_{y,i}^2, \\ I_{p,k,y_k} &= I_{k,y_k} + \sum_{i \in \mathcal{I}_k} m_i \tilde{d}_{x,i}^2. \end{aligned} \tag{4}$$

Here, $M_{p,k}$, $I_{p,k,x}$, and I_{p,k,y_k} refer to the intact region, whereas M_k, $I_{k,x}$, and I_{k,y_k} refer to the reconstructed region before adding the compensating masses. The offsets $\tilde{d}_{x,i}$ and $\tilde{d}_{y,i}$ are measured from the corresponding local centroidal axes. In this way, the reinforcement is used to recover the stiffnesses, while the discrete masses correct the remaining differences in mass and inertia. Details of the mass arrangement, calculated values, and fabrication approximations are reported in the Supplementary Text. Finite-element simulations were performed for intact, uncloaked, and reconstructed configurations with the seven two-opening regions. The first six transverse natural frequencies of the intact beam span 2.27–193.84 Hz. Over this range, the reconstructed frequencies differ from the intact values by less than 1.8%, and the difference remains below 0.25% for the first five modes. The same comparison can be expressed through the scattering reduction coefficient SRC = $|f^c - f^i|/|f^u - f^i|$, where f^i, f^u, and f^c are the natural frequencies of the intact, uncloaked, and reconstructed beams, respectively. The SRC ranges from 0 to 0.0231 for the first five transverse modes and increases to 0.1567 for the sixth mode. Frequency-response and transient simulations show the same trend: the reconstructed beam closely follows the intact response, while the untreated openings introduce clear frequency shifts and distort the propagating wave field (Supplementary Figs. S4–S8). Experiments were carried out on the uncloaked and reconstructed beams. The measured natural-frequency shifts agree closely with the numerical predictions (Supplementary Fig. S9). An intact beam was not included in the experimental campaign, so the near-intact equivalence is established numerically, while the experiments verify the predicted change from the uncloaked to the reconstructed configuration. The reconstruction was also tested numerically on a plate containing coupled flexural and torsional modes, where it continued to reduce the disturbance produced by the openings over the investigated frequency range (Supplementary Fig. S10). The two-opening design is important for the present metastructure because the structural reconstruction and the resonator integration are treated together. The crossbar provides the required clamping point, the large opening leaves space for the resonator motion, and the small opening gives access to the electrical connections. At the same time, the reinforcement and compensating masses recover the mechanical properties removed from the host. The resonators can therefore be embedded inside the beam without retaining the large dynamic changes produced by the untreated openings.

2.2 Coupling of magneto-elastic resonators with piezoelectric transducers

Piezoelectric cantilever resonators are embedded inside the cloaked voids and aligned parallel to the neutral axis of the host beam, with their mid-plane coincident with that of the host (Fig. 1B). Each resonator beam is made of carbon fiber and has effective dimensions $85 \times 24 \times 0.5$ mm^3. Two piezoelectric layers are bonded near the clamped end, where the bending strain is highest, on the upper and lower surfaces of the resonator. Their electrodes are connected to a dedicated electrical circuit with identical load resistance R_L, enabling local electromechanical conversion from resonator strain to harvested electrical output.

A pair of axially magnetized neodymium disc magnets is used to introduce tunable nonlinear stiffness. One magnet is attached to the free tip of each resonator through a 3D-printed holder, while an identical magnet is fixed to the host beam facing the resonator magnet with the same pole orientation, producing a repulsive interaction. The host-mounted magnet is attached to an adjustable holder, allowing the magnet spacing of each resonator to be prescribed independently. This arrangement mechanically programs the nonlinear restoring force of each resonator through the assigned magnet spacing.

The magnetic interaction is modeled using a dipole approximation, in which each permanent magnet is represented by a magnetic dipole with a prescribed magnetic moment (*55, 56*). This model provides a compact representation of the distance-dependent magnetic force and captures the monostable–bistable transition induced by changing the magnet spacing. The complete derivation is provided in the Supplementary Text. In the reduced-order model, the x-component of the magnetic force is neglected because the transverse dynamics of the j-th resonator are governed primarily by the z-component acting along the resonator deflection direction, as shown in Fig. 2A. The resulting magnetic force is

$$F_{Bj,z}\left(u_j(t)\right) = \frac{3\mu_0\mu_A\mu_B u_j(t)}{4\pi {r_j}^5 l}\left[e_j - \sqrt{l^2 - u_j(t)^2} - \frac{5e_j}{r_j^2}\left(u_j(t)^2 - e_j\sqrt{l^2 - u_j(t)^2}\right)\right] \quad (5)$$

where μ_0 is the vacuum permeability, μ_A and μ_B are the magnetic moments of dipoles A and B, $u_j(t)$ is the transverse displacement at the tip of the j-th resonator, and l is the effective distance from the resonator clamp to dipole A. The prescribed magnet spacing d_j defines the undeformed magnetic gap of the j-th resonator and enters the force through the displacement-dependent horizontal separation $e_j(u_j)$, while $r_j(u_j) = \sqrt{u_j(t)^2 + e_j(u_j)^2}$ is the center-to-center distance between the dipoles. Details of the magnetic-force derivation and geometric definitions are provided in the Supplementary Text.

Changing d_j reshapes the magneto-elastic potential of the resonator. Figure 2B shows the potential energy curves for different magnet spacings. At large spacing, the magnetic interaction is weak and the resonator remains monostable, with a single stable equilibrium (Fig. 2C-i). Reducing

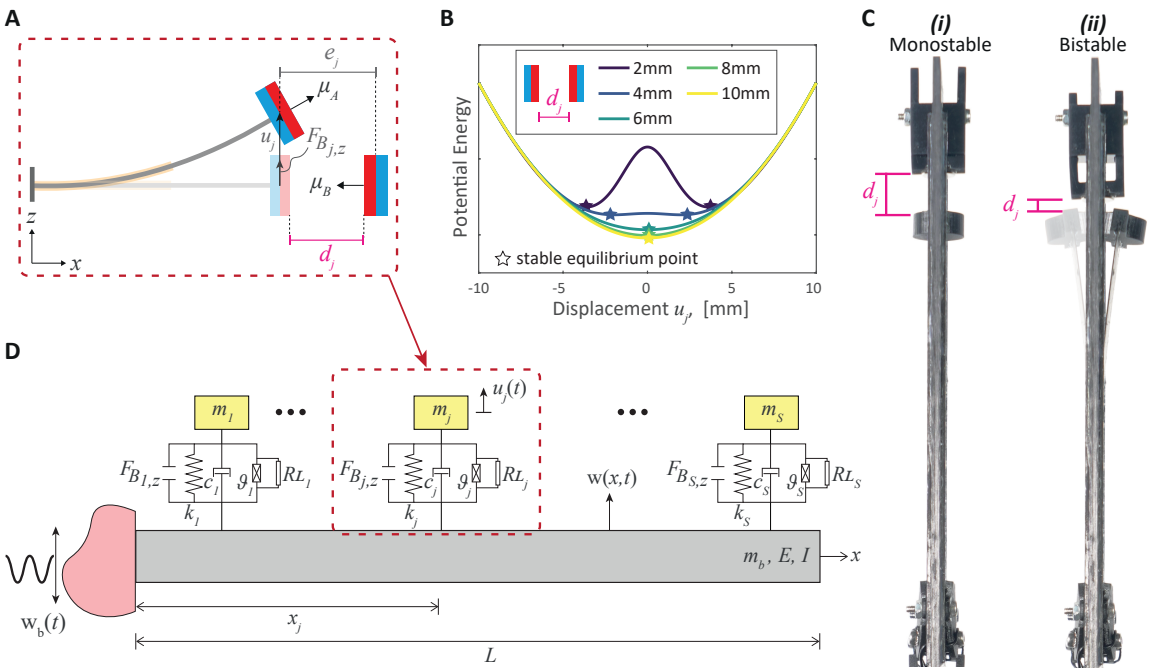


Figure 2: **Magneto-elastic piezoelectric resonators and reduced-order metabeam model**. (**A**) Schematic of the j-th resonator, showing the piezoelectric cantilever, the prescribed magnet spacing d_j, the displacement-dependent horizontal dipole separation e_j, and the transverse magnetic-force component $F_{B_j,z}$. (**B**) Magneto-elastic potential energy curves as a function of resonator displacement u_j for different prescribed magnet spacings d_j. Stable equilibrium positions are indicated. (**C**) Physical realizations of the j-th resonator in the (i) monostable ($d_j = 7$ mm) and (ii) bistable ($d_j = 3$ mm) configurations. (**D**) Reduced-order model of the metabeam with S embedded magneto-elastic piezoelectric resonators coupled to a continuous host beam under base excitation $w_b(t)$. Each resonator is represented by an effective mass m_j, stiffness k_j, damping c_j, nonlinear magnetic force $F_{B_j,z}$, electromechanical coupling ϑ_j and load resistance R_L.

the magnet spacing strengthens the repulsive interaction and transforms the resonator potential from a single-well to a double-well landscape, with two stable equilibrium positions separated by an unstable equilibrium (Fig. 2C-ii). The magnet spacing therefore determines whether the local potential is monostable or bistable.

A reduced-order electromechanical model is then developed for the complete metastructure under base excitation (Fig. 2D). The total transverse displacement of the host beam is written as $w_t(x,t) = w_b(t) + w(x,t)$, where $w_b(t)$ is the imposed base motion and $w(x,t)$ is the beam displacement relative to the base. Because the voids are elastically reconstructed, the host is modeled as an Euler–Bernoulli beam with viscous damping, while the embedded piezoelectric resonators are represented as lumped electromechanical oscillators attached at positions x_j. The coupled governing equations are

$$m_b \frac{\partial^2 \mathrm{w}}{\partial t^2}(x,t) + c\frac{\partial \mathrm{w}}{\partial t}(x,t) + EI\frac{\partial^4 \mathrm{w}}{\partial x^4}(x,t) - \sum_{j=1}^{S}\left(c_j \dot{u}_j(t) + k_j u_j(t) - F_{B_{j,z}}(u_j(t)) - \vartheta_j v_j(t)\right)\delta(x - x_j) = -m_b \ddot{\mathrm{w}}_b(t) \tag{6}$$

$$m_j \ddot{u}_j(t) + c_j \dot{u}_j(t) + k_j u_j(t) - F_{B_{j,z}}(u_j(t)) - \vartheta_j v_j(t) = -m_j\left[\frac{\partial^2 \mathrm{w}}{\partial t^2}(x_j,t) + \ddot{\mathrm{w}}_b(t)\right], \quad j = 1, 2, \ldots, S \tag{7}$$

$$Cp_j \dot{v}_j(t) + \mathcal{Y}_j v_j(t) + \vartheta_j \dot{u}_j(t) = 0, \quad j = 1, 2, \ldots, S \tag{8}$$

where $\delta(\cdot)$ is the Dirac delta function; u_j and v_j are the displacement and voltage of the j-th resonator; x_j is its position along the beam; m_b, c and EI are the mass per unit length, damping coefficient, and flexural rigidity of the host beam; m_j, c_j and k_j are the effective mass, damping coefficient, and linear stiffness of the j-th resonator; $F_{B_{j,z}}$ is the nonlinear magnetic force; ϑ_j is the electromechanical coupling coefficient; Cp_j is the equivalent piezoelectric capacitance; $\mathcal{Y}_j = 1/R_L$ is the load admittance; and S is the number of embedded resonators.

The beam displacement is expanded using the clamped-free mode shapes, and the governing equations are projected using the Galerkin method to obtain a finite-dimensional system of ordinary differential equations. The resulting electromechanical system is numerically integrated using a Runge–Kutta method. Details of the modal projection, matrix formulation, and numerical procedure are provided in the Supplementary Text.

2.3 Tunable response in metastructures with identical resonators

We first investigate metastructures in which all resonators are configured identically, with the same magnet spacing assigned to every resonator. Frequency up-sweep vibration tests were performed for magnet spacings ranging from 2 to 10 mm, in 1 mm increments, to determine how this single mechanical parameter reconfigures the vibration-attenuation and energy-harvesting spectra.

From the measured responses, we compute a power spectral density (PSD)-based velocity transmissibility T, obtained from the ratio between the velocity PSDs measured at the tip and base of the metabeam, as indicated in Fig. 3A. Figure 3B shows the experimental transmissibility as a function of frequency and magnet spacing. The gray-shaded region identifies the attenuation band, whereas the green curves mark its lower and upper frequency boundaries. Peaks in transmissibility indicate resonant amplification. Movies S2 and S3 illustrate the corresponding experimental responses.

Changing the magnet spacing modifies the local nonlinear potential of the resonators and therefore shifts the attenuation band. Figure 3C illustrates this effect through two identical configurations,

a monostable state with a magnet spacing of 7 mm and a bistable state with a magnet spacing of 3 mm. The full evolution of the bandgap boundaries with magnet spacing is summarized in Fig. 3D, where experimental and numerical results are compared across the tested identical configurations. The transition between monostable and bistable potentials occurs near a magnet spacing of 5 mm, consistent with the potential energy analysis.

The observed bandgap shifts can be understood from the curvature of the magneto-elastic potential around the equilibrium states accessed during the frequency sweep. In the monostable regime, reducing the magnet spacing strengthens the repulsive magnetic interaction around the central equilibrium. This reduces the local curvature of the potential and softens the effective restoring response of the resonators, lowering their resonant attenuation frequency. Consequently, the bandgap moves from approximately 40–55 Hz for the identical 10 mm configuration to 35–50 Hz for the identical 6 mm configuration. Once the resonators become bistable, the response under the tested excitation is governed by intrawell oscillations around one of the stable equilibria. Further reducing the magnet spacing increases the curvature of these wells, producing a stiffer intrawell response and shifting the attenuation region to higher frequencies. Accordingly, the bandgap changes from approximately 40–65 Hz for the identical 4 mm configuration to 62–80 Hz for the identical 3 mm configuration. Over the tested range, the bistable configurations also provide broader attenuation bandwidths than the monostable configurations. Numerical simulations reproduce the same shift in the attenuation bands. Additional numerical results are reported in the Supplementary Text.

Magnet spacing also reconfigures the harvested-power spectrum. Figure 3E shows the experimental total harvested-power PSD, obtained by summing the power contributions measured across the independent load resistances of the seven-resonator channels and normalizing by the squared input acceleration. The strongest spectral power occurs near the host-beam resonances, where host motion most effectively excites the embedded resonators. A secondary peak also appears inside the attenuation band, showing that electromechanical conversion persists even when vibration transmission through the host is suppressed. As the magnet spacing changes, the harvested-power spectrum shifts together with the attenuation response, demonstrating that the same mechanical parameter prescribes both suppression and conversion windows.

Figure 3F compares the total harvested-power PSD for the identical 7 mm monostable and identical 3 mm bistable configurations. The 7 mm monostable configuration produces the stronger peak response, with power concentrated near the host-beam resonance. The 3 mm bistable configuration distributes the harvested response over a broader frequency range, but with lower peak PSD levels under the tested excitation. This contrast reflects the different nonlinear restoring force prescribed by the magnet spacing. In the bistable regime, the stronger magnetic interaction creates a double-well potential, but interwell motion requires sufficiently large excitation energy. Under the present frequency-sweep conditions, the resonators remain confined to intrawell oscillations,

reducing their vibration amplitudes and, consequently, the harvested power. Even so, measurable harvested power persists within the attenuation bands of both programmed states. The same resonator motion that generates the locally resonant attenuation also strains the piezoelectric layers, so electrical conversion remains possible inside the attenuation band.

The identical-spacing tests show that changing **d** moves both the attenuation and harvested-power spectra. Changing **d** modifies the resonator dynamics and consequently shifts both responses in frequency. Therefore, the multifunctional response can be retuned without modifying the resonator architecture, structural layout, added mass, or external tuning elements.

The measured harvested power further places the energy-conversion response within a relevant range for low-power sensing. To illustrate this point, the identical 7 mm monostable configuration is considered under a fixed base-acceleration amplitude of 6 g. The measured total AC power dissipated in the independent load circuits reaches 10.67 μW near resonance at 29 Hz and 2.05 μW inside the bandgap at 41 Hz. Using the power-management estimate detailed in the Supplementary Text, with an illustrative conversion efficiency of 75%, these values correspond to estimated DC powers of approximately 8.0 μW and 1.54 μW, respectively, after rectification, storage, and regulation. These μW-level power budgets are comparable to the power consumption reported in the datasheets for operating modes of commercial ultra-low-power sensor ICs, such as the ADXL362 accelerometer and the HDC1080 and SHTC3 temperature–humidity sensors, as detailed in the Supplementary Text. This comparison supports the feasibility of duty-cycled sensing across distinct operating regimes, from high-response resonance to vibration-attenuating bandgap operation.

2.4 Impact of elastic invisibility on energy harvesting potential

We next examine whether the reconstructed wave field changes the mechanical energy delivered to the resonators. Elastic invisibility is central to this mechanism because it reduces the parasitic scattering introduced by the internal voids. In an uncloaked beam, the voids act as geometric discontinuities that scatter the incident elastic-wave field and perturb the background dynamics. In the cloaked beam, the reconstructed regions recover near-intact transmission. More of the propagating mechanical energy can therefore reach the embedded resonators.

To quantify wave-field preservation beyond modal frequencies, we evaluate the displacement-based scattering measure (*57*)

$$\varepsilon(u_1, u_2, \mathcal{R}) = \left(\int_{\mathcal{R}} |u_1(\mathbf{x}) - u_2(\mathbf{x})|^2 \, \mathrm{d}\mathbf{x} \right) \left(\int_{\mathcal{R}} |u_2(\mathbf{x})|^2 \, \mathrm{d}\mathbf{x} \right)^{-1}, \tag{9}$$

where $\mathcal{R}$ is the forward-scattering region shown in Fig. 3A, and $u_1(\mathbf{x})$ and $u_2(\mathbf{x})$ are the displacement fields under comparison. We compute $\varepsilon(u_u, u_i, \mathcal{R})$ and $\varepsilon(u_c, u_i, \mathcal{R})$, where u_c, u_u, and u_i denote the displacement fields of the cloaked, uncloaked, and intact beams, respectively, without embedded resonators. A perfectly cloaked structure satisfies $\varepsilon = 0$. We also define the relative scat-

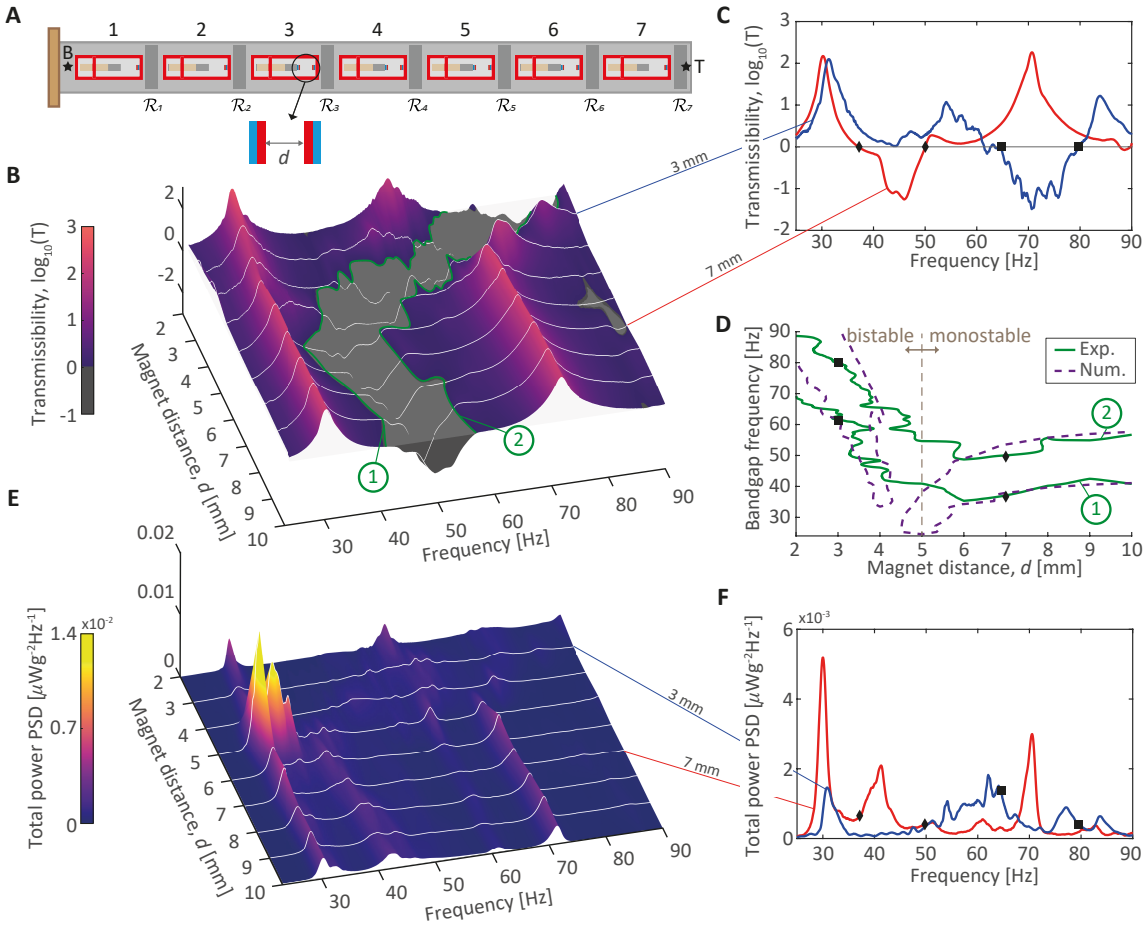


Figure 3: **Tunable attenuation and energy harvesting response under different magnet spacings**. (**A**) Schematic of the metastructure with seven embedded resonators and adjustable magnet spacing. The regions $\mathcal{R}i$ denote the forward-scattering regions used to evaluate wave scattering. (**B**) Experimental transmissibility, $\log_{10}(T)$, computed from the velocity PSD ratio between the tip (T) and base (B) locations indicated in Fig. 3A, shown as a function of frequency and magnet spacing. (**C**) Experimental transmissibility for the representative bistable and monostable cases with magnet spacings of 3 mm and 7 mm, respectively. Markers indicate the corresponding bandgap limits. (**D**) Bandgap boundaries as a function of magnet spacing, comparing experimental results with numerical simulations. The vertical dashed line indicates the approximate transition between bistable and monostable resonator regimes. (**E**) Experimental total harvested PSD, computed from the summed harvested power of the seven resonators and normalized by the squared input acceleration (where g is the gravitational acceleration), as a function of frequency and magnet spacing. (**F**) Total harvested power PSD for the representative 3 mm and 7 mm configurations.

tering reduction as $Q = |\varepsilon(u_u, u_i, \mathcal{R}) - \varepsilon(u_c, u_i, \mathcal{R})|/\varepsilon(u_u, u_i, \mathcal{R})$, where $Q = 1$ indicates complete reduction of the scattering introduced by the voids.

Across the seven forward-scattering regions and the tested frequencies, the cloaked beam exhibits substantially lower scattering than the uncloaked configuration, with most Q values exceeding 0.97 (Supplementary Fig. S11). This indicates that elastic reconstruction suppresses void-induced wave perturbations and restores near-intact transmission through the host beam. The restored background wave field also increases the mechanical energy delivered to the embedded resonators. When resonators are inserted into the cloaked beam, their total kinetic energy is approximately 7% higher than in the uncloaked beam. The largest gain occurs near the beam tip, where scattering effects accumulate along the propagation path, with the seventh resonator showing an energy enhancement of approximately 898% (Supplementary Figs. S12–S13). The reconstruction therefore has two quantifiable effects in the simulations: it recovers the background response and increases the kinetic energy of the embedded resonators.

2.5 Amplitude-dependent dynamics and onset of chaos

Nonlinear resonators can exhibit amplitude-dependent responses that strongly influence vibration attenuation and energy harvesting. We therefore examine how input acceleration modifies the metastructure response in bistable and monostable regimes, distinguishing conditions that favor enhanced energy conversion from those that preserve frequency-selective locally resonant attenuation.

Figure 4A shows the experimental transmissibility of the identical bistable configuration with a magnet spacing of 3 mm under input accelerations of 2 g, 6 g, and 9 g. At 2 g, the metastructure exhibits a clear attenuation band. Increasing the excitation amplitude progressively narrows this band, and at 9 g the well-defined attenuation region disappears, consistent with the emergence of large-amplitude irregular interwell motion observed in Movie S4. The transmissibility then remains nearly flat and close to unity over a broad frequency range, showing no pronounced elastic-wave attenuation or amplification.

To identify the resonator dynamics associated with this transition, we excite the metastructure at 71 Hz and apply the 0–1 test for chaos to the resonator time-series responses. The 0–1 test is a direct time-series method that distinguishes regular from chaotic dynamics by mapping the measured signal into transformed coordinates and evaluating the asymptotic growth of the corresponding trajectories (*58, 59*). The resulting classifier ranges from 0 to 1, with values below 0.2 indicating regular dynamics, values above 0.8 indicating chaos, and intermediate values considered inconclusive. Details of the implementation are provided in the Supplementary Text.

Figure 4B shows the 0–1 test results obtained from experimental and numerical resonator responses under different acceleration levels. At 2 g and 6 g, the responses remain regular, whereas at 9 g the classifier indicates chaotic dynamics. This transition is corroborated by the phase portrait and Poincaré map of resonator 1 in Figs. 4D,E, which show periodic motion at 6 g and scattered

Poincaré points at 9 g. Corresponding results for the remaining resonators, together with numerical validation, are reported in the Supplementary Text. These results provide mutually consistent evidence that the experimentally observed large-amplitude irregular interwell motion is associated with chaotic resonator dynamics.

This transition explains the disappearance of the locally resonant bandgap. At lower amplitudes, the resonators exhibit regular motion and interact with the host beam through a well-defined frequency-dependent dynamic impedance, producing a stable attenuation band. At 9 g, chaotic motion introduces broadband spectral content, nonperiodic dynamics, and loss of a coherent phase relation with the host beam (Supplementary Fig. S36). The resonators therefore no longer provide the stable dynamic interaction required to sustain locally resonant attenuation.

Figure 4C presents the total RMS-based harvested power for the bistable configuration. The harvested power increases markedly at 9 g, where the resonators exhibit chaotic motion. This enhancement is consistent with larger-amplitude excursions between potential wells, which increase the resonator strain available for piezoelectric conversion. At high amplitude, the bistable response therefore exchanges a well-defined attenuation band for larger harvested power.

The monostable configuration exhibits a markedly more robust amplitude response. Figure 4F shows the experimental transmissibility for the monostable configuration with a magnet spacing of 7 mm under input accelerations of 2 g, 6 g, and 9 g. In contrast to the bistable case, the attenuation band remains visible across all tested amplitudes, indicating weak amplitude dependence over this range. The 0–1 test results in Fig. 4G indicate regular dynamics in both experimental and numerical responses. This regular behavior is further supported by the phase portrait and Poincaré map in Figs. 4I,J, which confirm periodic motion. The harvested-power response in Fig. 4H varies much less strongly with acceleration than in the bistable configuration.

The amplitude response is consequently very different in the two potential landscapes. Bistable dynamics can enhance energy harvesting through large-amplitude chaotic interwell motion, whereas monostable dynamics preserve a more stable attenuation response over the tested acceleration range.

2.6 Enhanced performance using nonidentical resonator programming

Nonidentical configurations extend the mechanical programming strategy by allowing the magnet spacing of each embedded resonator to be prescribed independently. The seven resonators can therefore occupy different nonlinear states, with the overall configuration defined by the magnet spacing vector $\mathbf{d}_i = [d_1, \ldots, d_j, \ldots, d_7]$, where d_j denotes the spacing assigned to the j-th resonator in the i-th configuration. Each vector $\mathbf{d}_i$ thus specifies the spatial distribution of magneto-elastic potentials along the metastructure. With discrete spacings ranging from 2 to 10 mm in 1 mm increments, the seven-resonator array admits 9^7 possible magnet spacing vectors. This substantially enlarges the design space available for exploring the two performance metrics.

To experimentally sample this design space, we selected seven nonidentical configurations that

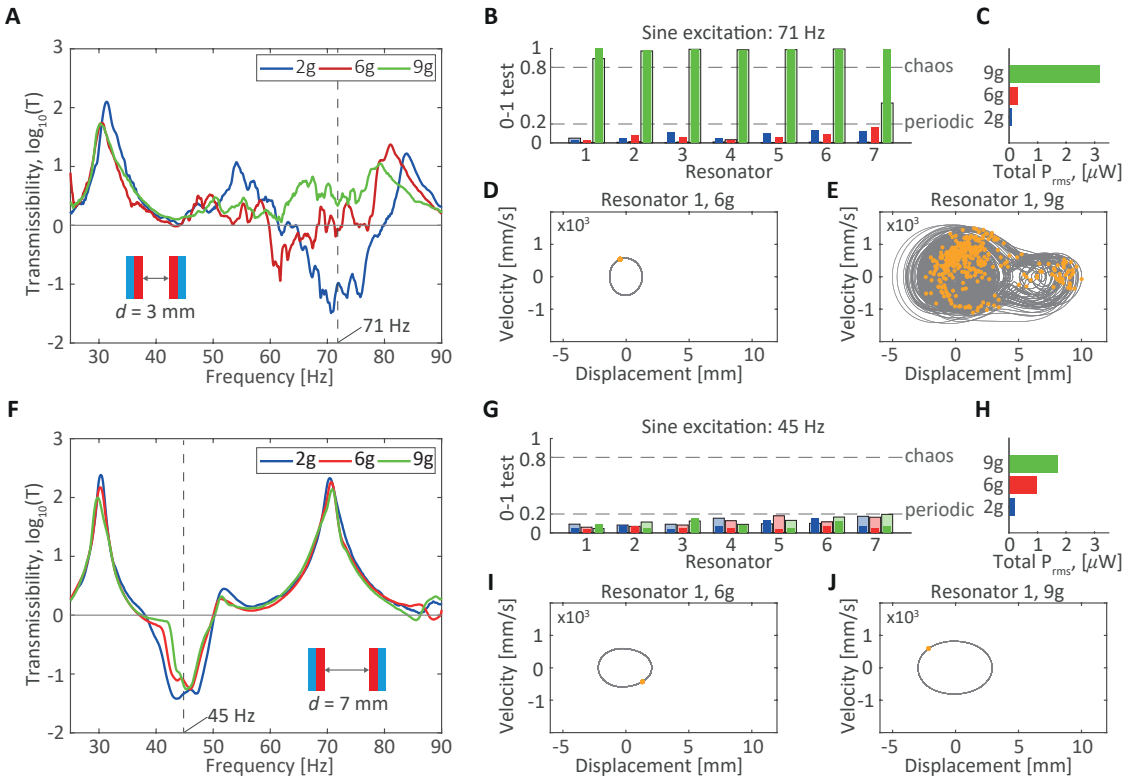


Figure 4: **Amplitude-dependent dynamics of the metastructure**. (**A**) Experimental transmissibility of the bistable configuration with a magnet spacing of 3 mm under input accelerations of 2 g, 6 g, and 9 g. (**B**) 0–1 test for chaos applied to the seven resonator responses under fixed-frequency sine excitation at 71 Hz, selected inside the attenuation band observed at lower amplitudes. Solid bars are obtained from experimental time series, and faded bars are obtained from numerical time series. (**C**) Total harvested power estimated from the RMS voltages of the seven resonators for the bistable configuration under fixed-frequency sine excitation at 71 Hz. (**D**,**E**) Experimental phase portraits of resonator 1 in the bistable configuration under 6 g and 9 g, respectively. Orange dots denote the corresponding Poincaré points. (**F**) Experimental transmissibility of the monostable configuration with a magnet spacing of 7 mm under input accelerations of 2 g, 6 g, and 9 g. (**G**) 0–1 test for chaos applied to the seven resonator responses under fixed-frequency sine excitation at 45 Hz, selected inside the attenuation band. Solid and faded bars denote experimental and numerical time-series results, respectively. (**H**) Total harvested power estimated from the RMS voltages of the seven resonators for the monostable configuration under fixed-frequency sine excitation at 45 Hz. (**I**,**J**) Experimental phase portraits of resonator 1 in the monostable configuration under 6 g and 9 g, respectively. Orange dots denote the corresponding Poincaré points.

combine magnet spacings from distinct nonlinear regimes (Fig. 5A-B). N1–N3 group the 3 mm bistable and 7 mm monostable states in different longitudinal regions of the resonator array, N4 and N5 alternate these two states, and N6 and N7 impose graded prescriptions from 2 to 8 mm and from 8 to 2 mm, respectively. The seven configurations therefore cover grouped, alternating, and graded spacing patterns.

Figure 5C summarizes all tested prescriptions in a normalized attenuation–harvesting performance map. For each configuration, the harvesting metric A_P is computed as the area of the total harvested-power PSD over the tested frequency range, while the attenuation metric B is defined as the corresponding attenuation bandwidth. The coordinates $A_P/A_{P,7\mathrm{mm}}$ and $B/B_{3\mathrm{mm}}$ normalize these metrics by using two identical-spacing references. The 7 mm monostable case is used as the harvesting reference, whereas the 3 mm bistable case is used as the attenuation reference. These configurations provide representative harvesting- and attenuation-favored baselines, respectively.

The map also includes the identical configurations, labeled as I2-I10, where the number indicates the common magnet spacing in millimeters. Among the identical configurations, I5 provides the largest harvesting response, reaching $A_P/A_{P,7\mathrm{mm}} = 1.57$, whereas the largest attenuation bandwidths are obtained for I2 and I4, with $B/B_{3\mathrm{mm}} = 1.07$ and 1.06, respectively. I5 also provides the highest harvesting performance among all experimentally tested configurations.

The experimental nonidentical configurations occupy distinct regions of the performance map, demonstrating that the prescribed magnet spacing vector strongly modifies the multifunctional response. N1, N2, N5, N6, and N7 exceed the attenuation-bandwidth reference, with $B/B_{3\mathrm{mm}} > 1$. N5 provides the largest attenuation bandwidth among all experimentally tested configurations, reaching $B/B_{3\mathrm{mm}} = 1.82$ while retaining $A_P/A_{P,7\mathrm{mm}} = 0.59$. In contrast, N4 provides the strongest harvesting response among the nonidentical configurations, reaching $A_P/A_{P,7\mathrm{mm}} = 0.95$ while maintaining $B/B_{3\mathrm{mm}} = 0.83$. The contrast between N4 and N5 is particularly informative because both alternate 3 and 7 mm spacings, but differ in the number of resonators assigned to each spacing and in their positions along the array. Their different positions in the map show that performance depends not only on how many resonators use each state, but also on where those states are placed.

This sensitivity to ordering arises from the spatial variation of the vibration field along the host beam, which causes each resonator to experience a distinct local amplitude and phase. Resonators near nodal or low-motion regions of the relevant mode shapes are weakly activated and contribute less to attenuation and piezoelectric conversion, whereas resonators in high-motion regions can dominate the multifunctional response. A resonator assigned the same magnet spacing can therefore behave differently at different positions because its local excitation amplitude is different. The nonidentical configurations make use of this spatial dependence by placing different magnet spacings at different positions along the beam.

Figure 5D shows that nonidentical configurations produce multiple attenuation regions, indicating that the attenuation band can be reshaped by prescribing the magnet spacing sequence. The

transmissibility curves in Fig. 5E show that N4 and N5 generate different attenuation intervals despite using the same two magnet spacing states. The total power PSDs in Fig. 5F show that changing this alternating prescription reshapes the harvested-power spectrum. Because the 7 mm monostable state contributes mainly to the lower-frequency response, whereas the 3 mm bistable state contributes mainly to the higher-frequency response, changing the number and positions of resonators assigned to each state along the beam redistributes the harvested power between these spectral regions. Accordingly, N4 produces stronger power in the lower-frequency region, while N5 produces stronger power in the higher-frequency region. The measurements therefore show that the spacing sequence changes both the attenuation intervals and the distribution of harvested power across frequency.

The model-predicted candidates in Fig. 5C extend the experimental trend toward improved attenuation–harvesting balance. Their normalized performances follow the same reference logic as the experiments, using the numerical identical 3 mm and 7 mm configurations as attenuation- and harvesting-favored references, respectively. The selected candidates are labeled P1–P4 in the performance map and correspond to the magnet spacing vectors P1=[4,5,5,5,7,3,2], P2=[4,5,7,7,3,3,2], P3=[7,5,3,7,3,5,2], and P4=[7,5,3,7,3,7,2]. P1 contains several 5 mm states near the monostable–bistable transition, where reduced effective stiffness favors large resonator motion and harvesting but limits attenuation bandwidth. Replacing part of these transition states with 7 mm and 3 mm states in P2 increases the attenuation bandwidth at the expense of harvested power. The calibrated model predicts that P3 and P4, which combine 2-3-5-7 mm states along the array, lie within the region of the numerical performance map where both performance metrics are simultaneously improved. The predicted P3 and P4 cases suggest that further improvement may be obtained by searching the spacing-vector design space without changing the beam architecture.

3 Conclusion

We have developed and experimentally assessed an elastic-invisibility-enabled metastructure that embeds nonlinear magneto-elastic piezoelectric resonators inside a structural host beam for simultaneous vibration attenuation and energy harvesting. Numerical comparisons among the intact, uncloaked, and cloaked beams show that the elastic reconstruction strongly suppresses the perturbations introduced by the internal voids and recovers a near-intact dynamic response. Experiments on the cloaked and uncloaked beams confirm the modal shifts predicted by the numerical model. Near-intact equivalence is therefore established numerically, while the experiments confirm the predicted changes between the uncloaked and reconstructed beams. The reconstructed openings can therefore house the resonators without introducing the large dynamic perturbations associated with the untreated voids. Here, the cloaking concept is used for functional integration: the reconstruction compensates for the openings required to embed the resonators.

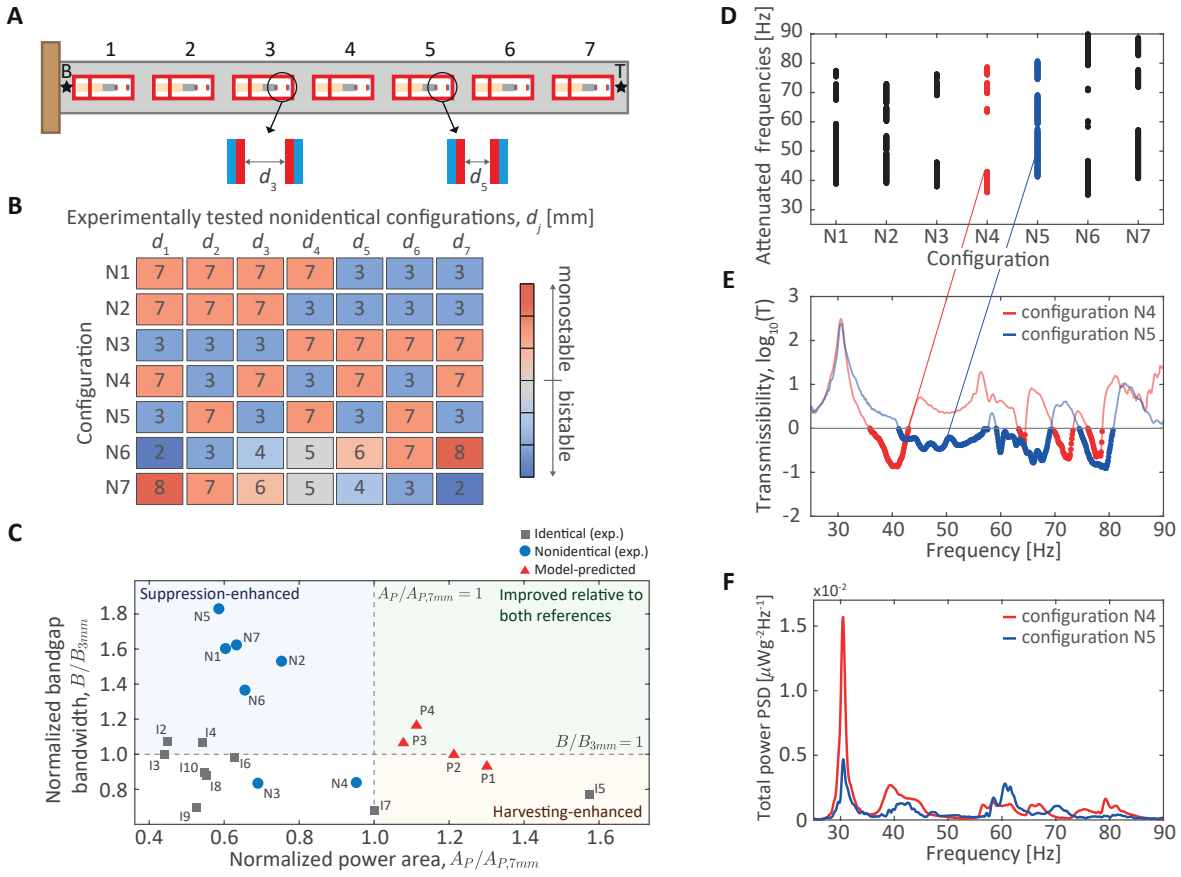


Figure 5: **Mechanically programmed attenuation–harvesting performance with nonidentical magnet spacing prescriptions**. (**A**) Schematic of the metastructure with independently prescribed magnet spacings assigned to the seven embedded resonators. (**B**) Experimentally tested nonidentical configurations. (**C**) Normalized attenuation–harvesting performance map. Each configuration is represented by $A_P/A_{P,7\text{mm}}$ and $B/B_{3\text{mm}}$, where A_P is the area of the total power PSD over the tested frequency range and B is the attenuation bandwidth. The normalization references $A_{P,7\text{mm}}$ and $B_{3\text{mm}}$ correspond to the metric values of the identical 7 mm monostable and 3 mm bistable configurations, respectively. Gray squares denote experimental identical configurations, blue circles denote experimental nonidentical configurations, and red triangles denote model-predicted candidates. (**D**) Experimental attenuation regions for the tested nonidentical configurations. (**E**) Experimental transmissibility of configurations N4 and N5. (**F**) Experimental total power PSD of configurations N4 and N5.

Local mechanical programming is achieved through the magneto-elastic interaction of each resonator. Changing only the magnet spacing switches the local potential between monostable and bistable forms and shifts both the attenuation and harvesting responses. The experiments reveal how amplitude controls the functional regime of the metastructure. Regular bistable intrawell motion supports locally resonant attenuation, whereas high-amplitude chaotic interwell motion enhances energy conversion while disrupting bandgap stability. Monostable configurations preserve a more regular and amplitude-robust attenuation response over the tested range. Nonidentical spacing patterns further redistribute attenuation and harvested power across frequency, showing that multifunctional performance can be programmed through the magnet spacing vector. The experimental and model-predicted configurations indicate that the spacing-vector design space can be used to seek configurations that perform well in both metrics.

The metastructure generates measurable electrical power under resonant energy concentration and under vibration-suppression conditions, while elastic reconstruction preserves the effective dynamics of the structural host. The main distinction of the present design is that the resonators are embedded inside the host while the mechanical properties lost when the openings are created are restored. Their nonlinear state can then be changed independently through magnet spacing. The concept can be extended to other geometries and frequency ranges by redesigning the elastic reconstruction, resonator tuning, and transduction mechanism for the target structure. Future versions could further improve electrical output through load optimization, rectification, storage and phase-aware power electronics. A longer-term extension would be to use stored harvested energy to drive an adjustable magnet-spacing mechanism, enabling closed-loop reconfiguration.

4 Materials and Methods

Fabrication and assembly

The host beam, with dimensions $985 \times 45 \times 2$ mm^3, contains seven equally spaced rectangular voids of 118×30 mm^2. The beam, elastic-reconstruction frames, and cantilever resonators (dimensions $85 \times 24 \times 0.5$ mm^3) were fabricated from carbon fiber, selected for its low density, low structural damping, flexibility, and non-ferromagnetic character. All components were machined by CNC milling. The reconstruction frames and compensating masses were bonded to the host beam using a structural epoxy adhesive (3M Scotch-Weld DP460), after which the seven cantilever resonators were installed within the reconstructed regions. Each resonator carries two piezoelectric patches (S118-J1SS-1808YB, Mide Technology) bonded near the clamped end, where the bending strain is highest. The patches on each resonator were connected in parallel to an independent resistive load. The seven resonators are therefore mechanically coupled through the host beam but electrically separated into individual harvesting channels. The nonlinear magnetic interaction was introduced

using a pair of identical neodymium disc magnets. One magnet was fixed to the resonator tip through a 3D-printed holder, while the second was mounted on an adjustable holder attached to the host beam. The magnets were aligned with approximately collinear magnetization axes and with equal-polarity faces opposing each other, producing a repulsive interaction. The adjustable holder allowed the magnet spacing of each resonator to be set independently. Additional fabrication details, dimensions, and assembly procedures are provided in the Supplementary Text and Movie S6.

Experimental setup

The metabeam was clamped to an electrodynamic shaker (TIRA vib 51144) mounted on an optical table (Nexus Optical Table, Thorlabs). Frequency up-sweep tests were performed over the 25–90 Hz range by imposing controlled translational base excitation on the metastructure. Fixed-frequency harmonic tests were also performed at selected operating conditions to evaluate the metabeam response and LED activation. The excitation was controlled using a VR9500 vibration controller with four channels and 26000 lines of resolution, operated through Vibration View software. An accelerometer (PCB 356A45) mounted at the base of the metabeam provided the feedback signal for the controller. The full-field displacement response was measured using a 3D digital image correlation system composed of two high-speed cameras (Photron Fastcam Nova S9), as shown in Movie S5. The voltage generated by each resonator was measured across its independent load resistance using an analog data acquisition system.

The vibration response was quantified using a PSD-based velocity transmissibility between the tip and the base of the metabeam, $T(f) = S_{\dot{w}_T}(f)/S_{\dot{w}_B}(f)$, where $S_{\dot{w}_T}(f)$ and $S_{\dot{w}_B}(f)$ are the velocity PSDs at the tip and base, respectively. The transmissibility was reported as $\log_{10}(T)$, and attenuation bands were identified from the frequency intervals satisfying $\log_{10}(T) < -0.05$. For energy harvesting analysis, the voltage PSD of each resonator channel was converted into harvested-power PSD by dividing by the corresponding load resistance. The normalized total harvested-power PSD was then obtained by summing the seven independent power contributions and normalizing by the squared base-acceleration amplitude. Further details on the experimental procedures, signal processing, and fixed-frequency tests are provided in the Supplementary Text.

Numerical simulations

The elastic-reconstruction geometry and compensating masses were determined in MATLAB by solving the stiffness, mass, and mass moment of inertia equivalence conditions. The reinforcement dimensions were obtained by minimizing the normalized residuals of the flexural and torsional stiffness conditions, after which the compensating masses were calculated to satisfy the corresponding mass and mass moment of inertia equivalence conditions. Full details of the numerical procedure are provided in the Supplementary Text. The reconstructed-beam response was then validated by

finite-element simulations in ABAQUS and compared with experimental measurements. Numerical simulations of the complete metastructure were performed in MATLAB using the nonlinear electromechanical model detailed in the Supplementary Text. The simulations were configured to match the experimental conditions, including magnet spacing configurations, load resistances, base-acceleration levels, and frequency range. Numerical outputs were processed using the attenuation and energy harvesting metrics consistent with the experimental analysis, enabling direct comparison between measured and simulated transmissibility, bandgap boundaries, and harvested-power responses. Additional details on the governing equations, numerical integration procedure, and parameter values are reported in the Supplementary Text.

Funding: J.P.N, A.C., and D.M acknowledge financial support from the European Union, ERC grant HE GA 101086644 S-FOAM. J.P.N. gratefully acknowledges financial support from Coordination for the Improvement of Higher Education Personnel (CAPES), grants 88887.677991/2022-00 and 88881.846270/2023-01. A.C. acknowledges financial support from the National Institute of Science and Technology - Smart Structures in Engineering (INCT-EIE), grant 406148/2022-8, National Council for Scientific and Technology Development (CNPq), grants 305476/2022-0, and Carlos Chagas Filho Research Foundation of Rio de Janeiro State (FAPERJ), grant 204.247/2024. Views and opinions expressed are however those of the author(s) only and do not necessarily reflect those of the European Union or the European Research Council Executive Agency. Neither the European Union nor the granting authority can be held responsible for them.

Author contributions: J.P.N., A.C., and D.M. developed the concept. J.P.N. and D.M. designed and fabricated the structure and performed the experiments. J.P.N., A.C., and D.M. developed the theoretical models and numerical simulations. All authors contributed to data analysis and manuscript writing. J.P.N. and D.M. created the figures and videos. All authors contributed to the Methods and Supplementary Information.

Competing interests: The authors declare no competing interests.

Data and materials availability: All data and simulation outputs were generated at the Laboratory of Design of Metamaterials and Structures, DICAM, University of Trento, where the physical samples are also retained.

References and Notes

1. W. Liu, *et al.*, Integrated charge excitation triboelectric nanogenerator. *Nature Communications* **10**, 1426 (2019), doi:10.1038/s41467-019-09464-8.

2. Y. Zhang, *et al.*, Rotational electromagnetic energy harvester for human motion application at low frequency. *Applied Physics Letters* **116** (5), 053902 (2020), doi:10.1063/1.5142575.

3. T. Zhang, *et al.*, Piezoelectric ultrasound energy–harvesting device for deep brain stimulation and analgesia applications. *Science Advances* **8** (15), eabk0159 (2022), doi:10.1126/sciadv.abk0159.

4. H. Zhao, X. Liu, Y. Li, Architecture Design of High-Performance Piezoelectric Energy Harvester with 3D Metastructure Substrate. *Advanced Theory and Simulations* **7** (10), 2301214 (2024), doi:10.1002/adts.202301214.

5. Z.-Q. Lu, *et al.*, Ocean wave energy harvesting with high energy density and self-powered monitoring system. *Nature Communications* **15** (6513) (2024), doi:10.1038/s41467-024-50926-5.

6. F. Kronowetter, *et al.*, Exceptional energy harvesting from coupled bound states. *Nature Communications* **16** (3515) (2025), doi:10.1038/s41467-025-58831-1.

7. M. Moccia, G. Castaldi, S. Savo, Y. Sato, V. Galdi, Independent Manipulation of Heat and Electrical Current via Bifunctional Metamaterials. *Phys. Rev. X* **4**, 021025 (2014), doi:10.1103/PhysRevX.4.021025.

8. X. Zheng, *et al.*, Ultralight, ultrastiff mechanical metamaterials. *Science* **344** (6190), 1373–1377 (2014), doi:10.1126/science.1252291.

9. J. Kim, S. Torquato, Multifunctional composites for elastic and electromagnetic wave propagation. *Proceedings of the National Academy of Sciences* **117** (16), 8764–8774 (2020), doi:10.1073/pnas.1914086117.

10. T. Chen, M. Pauly, P. M. Reis, A reprogrammable mechanical metamaterial with stable memory. *Nature* **589**, 386–390 (2021), doi:10.1038/s41586-020-03123-5.

11. A. Bossart, D. M. J. Dykstra, J. van der Laan, C. Coulais, Oligomodal metamaterials with multifunctional mechanics. *Proceedings of the National Academy of Sciences* **118** (21), e2018610118 (2021), doi:10.1073/pnas.2018610118.

12. Y. Zhang, A. Deshmukh, K.-W. Wang, Embodying Multifunctional Mechano-Intelligence in and Through Phononic Metastructures Harnessing Physical Reservoir Computing. *Advanced Science* **10** (34), 2305074 (2023), doi:10.1002/advs.202305074.

13. X. Xing, L. Wu, X. Tian, D. Li, Multifunctional Metamaterials with Ultrawideband Wave Absorption and Thermal Camouflage. *Advanced Engineering Materials* **25** (16), 2300389 (2023), doi:10.1002/adem.202300389.

14. P. Jiao, J. Mueller, J. Raney, X. Zheng, A. Alavi, Mechanical metamaterials and beyond. *Nature Communications* **14**, 6004 (2023), doi:10.1038/s41467-023-41679-8.

15. W. Liu, S. Janbaz, D. Dykstra, B. Ennis, C. Coulais, Harnessing plasticity in sequential metamaterials for ideal shock absorption. *Nature* **634**, 842–847 (2024), doi:10.1038/s41586-024-08037-0.

16. G. Lee, W. Choi, H. M. Seung, S. Kim, J. Rho, Synthesized dispersion-engineered elastic metasurfaces for achromatic focusing and harvesting across the audible to ultrasound ranges. *Proceedings of the National Academy of Sciences* **122** (18), e2425407122 (2025), doi:10.1073/pnas.2425407122.

17. Z. Liu, *et al.*, Locally Resonant Sonic Materials. *Science* **289** (5485), 1734–1736 (2000), doi:10.1126/science.289.5485.1734.

18. G. Ma, P. Sheng, Acoustic metamaterials: From local resonances to broad horizons. *Science Advances* **2** (2), e1501595 (2016), doi:10.1126/sciadv.1501595.

19. B. Wu, *et al.*, Wave Manipulation in Intelligent Metamaterials: Recent Progress and Prospects. *Advanced Functional Materials* **34** (29), 2316745 (2024), doi:10.1002/adfm.202316745.

20. J. Park, G. Lee, H. Kwon, M. Kim, J. Rho, All-Polarized Elastic Wave Attenuation and Harvesting via Chiral Mechanical Metamaterials. *Advanced Functional Materials* **34** (39), 2403550 (2024), doi:10.1002/adfm.202403550.

21. J. Hyun, J. Jung, J. Park, W. Choi, M. Kim, Simultaneous low-frequency vibration isolation and energy harvesting via attachable metamaterials. *Nano Convergence* **11** (38) (2024), doi:10.1186/s40580-024-00445-2.

22. X. Xu, *et al.*, Multifunctional Metamaterials for Energy Harvesting and Vibration Control. *Advanced Functional Materials* **32**, 2107896 (2022), doi:10.1002/adfm.202107896.

23. Z.-Q. Lu, L. Zhao, H. Ding, L.-Q. Chen, A dual-functional metamaterial for integrated vibration isolation and energy harvesting. *Journal of Sound and Vibration* **509**, 116251 (2021), doi:10.1016/j.jsv.2021.116251.

24. C. Xu, S. Chen, C. H. Wang, Y. Yang, L. Zhao, Amplitude-robust metastructure with combined bistable and monostable mechanisms for simultaneously enhanced vibration suppression and energy harvesting. *Applied Physics Letters* **122** (15), 151701 (2023), doi:10.1063/5.0136134.

25. C. Xu, Y. Yang, C. H. Wang, L. Zhao, Simultaneous low-frequency vibration suppression and energy harvesting using a metastructure with alternately combined nonlinear local resonators.

Mechanical Systems and Signal Processing **211**, 111241 (2024), doi:10.1016/j.ymssp.2024.111241.

26. K. Mikoshiba, J. M. Manimala, C. Sun, Energy harvesting using an array of multifunctional resonators. *Journal of Intelligent Material Systems and Structures* **24** (2), 168–179 (2013), doi:10.1177/1045389X12460335.

27. Y. Li, E. Baker, T. Reissman, C. Sun, W. K. Liu, Design of mechanical metamaterials for simultaneous vibration isolation and energy harvesting. *Applied Physics Letters* **111** (25), 251903 (2017), doi:10.1063/1.5008674.

28. C. Sugino, Y. Xia, S. Leadenham, M. Ruzzene, A. Erturk, A general theory for bandgap estimation in locally resonant metastructures. *Journal of Sound and Vibration* **406**, 104–123 (2017), doi:10.1016/j.jsv.2017.06.004.

29. S. El-Borgi, *et al.*, Multiple bandgap formation in a locally resonant linear metamaterial beam: Theory and experiments. *Journal of Sound and Vibration* **488**, 115647 (2020), doi:10.1016/j.jsv.2020.115647.

30. Y. Xia, M. Ruzzene, A. Erturk, Dramatic bandwidth enhancement in nonlinear metastructures via bistable attachments. *Applied Physics Letters* **114** (9), 093501 (2019), doi:10.1063/1.5066329.

31. Y. Xia, M. Ruzzene, A. Erturk, Bistable attachments for wideband nonlinear vibration attenuation in a metamaterial beam. *Nonlinear Dynamics* **102**, 1285–1296 (2020), doi:10.1007/s11071-020-06008-4.

32. V. Zega, P. B. Silva, M. G. D. Geers, V. G. Kouznetsova, Experimental proof of emergent subharmonic attenuation zones in a nonlinear locally resonant metamaterial. *Scientific Reports* **10** (12041) (2020), doi:10.1038/s41598-020-68894-3.

33. I. Kovacic, Z. Rakaric, Z. Kanovic, V. Rajs, Metastructure with integrated internal oscillators of constant, linearly and nonlinearly varying natural frequency. *Frontiers in Physics* **10** (2022), doi:10.3389/fphy.2022.934998.

34. D. Schurig, *et al.*, Metamaterial Electromagnetic Cloak at Microwave Frequencies. *Science* **314** (5801), 977–980 (2006), doi:10.1126/science.1133628.

35. S. A. Cummer, *et al.*, Scattering Theory Derivation of a 3D Acoustic Cloaking Shell. *Phys. Rev. Lett.* **100**, 024301 (2008), doi:10.1103/PhysRevLett.100.024301.

36. E. D. Sanders, M. A. Aguiló, G. H. Paulino, Optimized lattice-based metamaterials for elastostatic cloaking. *Proceedings of the Royal Society A: Mathematical, Physical and Engineering Sciences* **477** (2253), 20210418 (2021), doi:10.1098/rspa.2021.0418.

37. F. V. Senhora, E. D. Sanders, G. H. Paulino, Unbiased mechanical cloaks. *Proceedings of the National Academy of Sciences* **122** (19), e2415056122 (2025), doi:10.1073/pnas.2415056122.

38. F. Cottone, H. Vocca, L. Gammaitoni, Nonlinear Energy Harvesting. *Physical Review Letters* **102**, 080601 (2009), doi:10.1103/PhysRevLett.102.080601.

39. A. Erturk, J. Hoffmann, D. Inman, A piezomagnetoelastic structure for broadband vibration energy harvesting. *Applied Physics Letters* **94**, 254102 (2009), doi:10.1063/1.3159815.

40. H.-C. Song, *et al.*, Piezoelectric Energy Harvesting Design Principles for Materials and Structures: Material Figure-of-Merit and Self-Resonance Tuning. *Advanced Materials* **32** (51), 2002208 (2020), doi:10.1002/adma.202002208.

41. Y. Jia, Review of nonlinear vibration energy harvesting: Duffing, bistability, parametric, stochastic and others. *Journal of Intelligent Material Systems and Structures* **31** (7), 921–944 (2020), doi:10.1177/1045389X20905989.

42. X. Fang, J. Wen, B. Bonello, J. Yin, D. Yu, Ultra-low and ultra-broad-band nonlinear acoustic metamaterials. *Nature Communications* **8** (1288) (2017), doi:10.1038/s41467-017-00671-9.

43. X. Fang, J. Wen, B. Bonello, J. Yin, D. Yu, Wave propagation in one-dimensional nonlinear acoustic metamaterials. *New Journal of Physics* **19** (5), 053007 (2017), doi:10.1088/1367-2630/aa6d49.

44. S. M. Montgomery, *et al.*, Magneto-Mechanical Metamaterials with Widely Tunable Mechanical Properties and Acoustic Bandgaps. *Advanced Functional Materials* **31** (3), 2005319 (2021), doi:10.1002/adfm.202005319.

45. Y. Cao, M. Derakhshani, Y. Fang, G. Huang, C. Cao, Bistable Structures for Advanced Functional Systems. *Advanced Functional Materials* **31** (45), 2106231 (2021), doi:10.1002/adfm.202106231.

46. K. L. Tsakmakidis, A. D. Boardman, O. Hess, 'Trapped rainbow' storage of light in metamaterials. *Nature* **450**, 397–401 (2007), doi:10.1038/nature06285.

47. H. Li, Z. Luo, L. Gao, P. Walker, Topology optimization for functionally graded cellular composites with metamaterials by level sets. *Computer Methods in Applied Mechanics and Engineering* **328**, 340–364 (2018), doi:10.1016/j.cma.2017.09.008.

48. M. Alshaqaq, A. Erturk, Graded multifunctional piezoelectric metastructures for wideband vibration attenuation and energy harvesting. *Smart Materials and Structures* **30** (1), 015029 (2020), doi:10.1088/1361-665X/abc7fa.

49. C. Lan, G. Hu, L. Tang, Y. Yang, Energy localization and topological protection of a locally resonant topological metamaterial for robust vibration energy harvesting. *Journal of Applied Physics* **129** (18), 184502 (2021), doi:10.1063/5.0047965.

50. N. Jiménez, V. Romero-García, V. Pagneux, J. Groby, Rainbow-trapping absorbers: Broadband, perfect and asymmetric sound absorption by subwavelength panels for transmission problems. *Scientific Reports* **7** (13595) (2017), doi:10.1038/s41598-017-13706-4.

51. L. Zhou, W. Yu, Visualization of rainbow trapping effect in higher-order topological insulators. *Phys. Rev. B* **107**, 174105 (2023), doi:10.1103/PhysRevB.107.174105.

52. Z.-Q. Lu, *et al.*, Broadband acoustic signal sensing using an adaptive metamaterial. *Device* **3** (12), 100938 (2025), doi:10.1016/j.device.2025.100938.

53. D. Misseroni, A. B. Movchan, D. Bigoni, Omnidirectional flexural invisibility of multiple interacting voids in vibrating elastic plates. *Proceedings of the Royal Society A: Mathematical, Physical and Engineering Sciences* **475** (2229), 20190283 (2019), doi:10.1098/rspa.2019.0283.

54. S. Timoshenko, S. Woinowsky-Krieger, *Theory of plates and shells* (McGraw-Hill Book Company, New York) (2002).

55. J. Wen, *et al.*, Study of a Piezoelectric Energy Harvesting Collaborative Strategy Based on the Synergy of Multifrequency Technique and Magnetic Nonlinear Technique. *Advanced Engineering Materials* **25** (22), 2301154 (2023), doi:10.1002/adem.202301154.

56. D. Tan, Y. Leng, Y. Gao, Magnetic force of piezoelectric cantilever energy harvesters with external magnetic field. *The European Physical Journal Special Topics* **224**, 2839–2853 (2015), doi:10.1140/epjst/e2015-02592-6.

57. A. Movchan, N. Movchan, I. Jones, D. Colquitt, *Mathematical Modelling of Waves in Multi-Scale Structured Media*, Chapman & Hall/CRC Monographs and Research Notes in Mathematics (CRC Press) (2017).

58. G. A. Gottwald, I. Melbourne, A new test for chaos in deterministic systems. *Proceedings of the Royal Society of London. Series A: Mathematical, Physical and Engineering Sciences* **460** (2042), 603–611 (2004), doi:10.1098/rspa.2003.1183.

59. G. A. Gottwald, I. Melbourne, *The 0-1 Test for Chaos: A Review* (Springer Berlin Heidelberg, Berlin, Heidelberg), pp. 221–247 (2016), doi:10.1007/978-3-662-48410-4_7.

Supporting Information

Supplementary Text
Figures S1 to S40
Tables S1 to S7
Movies S1 to S6
References